Available online at www.sciencedirect.com

ScienceDirect

journal homepage: www.elsevier.com/locate/he

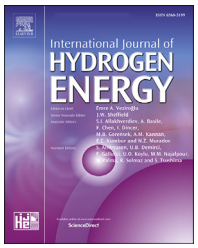

Grand canonical Monte Carlo simulations of the hydrogen and methane storage capacities of novel but MOFs at room temperature

I. Cabria

Departamento de Física Teórica, Atómica y Óptica, Universidad de Valladolid, 47011 Valladolid, Spain

HIGHLIGHTS

- Hydrogen Storage Capacities of Novel BUT MOFs.
- Methane Storage Capacities of Novel BUT MOFs.
- Volumetric capacities highly correlated with product porosity and isosteric heat.
- Three BUTs have high hydrogen gravimetric storage capacities.
- One BUT MOF, BUT-107, reaches the methane DOE targets.

ARTICLE INFO

Article history:
Received 17 April 2023
Received in revised form
21 June 2023
Accepted 26 June 2023
Available online 14 July 2023

Keywords:
Hydrogen storage
Methane storage
Metal-organic frameworks
Grand canonical Monte Carlo simulations

ABSTRACT

Hydrogen Fuel Cell Electric Vehicles (HFCEVs) and Natural Gas Vehicles (NGVs) are cleaner alternatives to present oil-based vehicles. The main problem of these technologies is the on-board storage. Metal-organic frameworks (MOFs) is one of the main groups of solid porous materials that can be used to store hydrogen or methane on-board these vehicles at room temperature and low or moderate pressures. The synthesis of these materials is usually expensive. Recently a group of eleven new BUT MOFs (BUT: Beijing University of Technology) has been synthesized using cheap organic precursors. Grand Canonical Monte Carlo simulations (GCMC) of the hydrogen and methane storage capacities and isosteric heats of these BUTs have been carried out and analyzed at 298.15 K and at pressures in the range 0.5–50 MPa. The correlations between the storage capacities and the porosity, the density, the pore size and the isosteric heat of the MOFs are analyzed. According to the simulations, three of the newly developed BUTs demonstrated high storage capacities for both hydrogen and methane. BUT-104 and 105 exhibited useable hydrogen volumetric and gravimetric capacities of approximately 0.023–0.027 kg/L and 4 wt % at 50 MPa. Additionally, they showcased useable methane volumetric and gravimetric capacities of 0.16–0.21 kg/L and 25 wt % at 25–35 MPa. Moreover, BUT-107 achieved the U.S. Department of Energy (DOE) hydrogen target for 2025, with a useable hydrogen gravimetric capacity of 5.5 wt % at 27 MPa. Furthermore, BUT-107 met the corresponding DOE methane targets, with useable methane volumetric and gravimetric capacities of 0.25 kg/L and 33.33 wt % at 50 MPa.

E-mail address: ivan.cabria@uva.es.

https://doi.org/10.1016/j.ijhydene.2023.06.298

Introduction

The emission of greenhouse gases is one of the main reasons of the climate change. Fossil fuel based road transport is the main responsible for the CO_2 emissions and pollution. The goal of the European Union for 2050 is to reduce the pollution from transport by 60%, compared to the year 1990 [1]. Hydrogen is a long-term and non-polluting alternative to the oil fuels. Road transport based on HFCEVs would reduce dependence on oil, pollution, and greenhouse gas emissions. Hydrogen has a very high specific energy, but a low energy density under normal conditions. This makes difficult the storage of hydrogen on-board of vehicles. Hence, it is relevant to investigate and find methods that store enough hydrogen. The technological goal is a hydrogen vehicle that has a range autonomy similar to that of fossil fuel based vehicles, about 600 km. To reach that goal, the DOE established specific on-board hydrogen storage targets: For 2020, 0.030 kg H_2/L and 4.5 wt % for the volumetric and gravimetric storage capacities, respectively, and for 2025, 0.040 kg/L and 5.5 wt %, respectively [2,3]. The ultimate storage targets are 0.050 kg H_2/L and 6.5 % wt. These values or targets correspond to the useable, also called delivery or working, capacities and also correspond to a reversible storage. One method to storage hydrogen is by compression on high pressure tanks. Hydrogen compressed storage systems at 70 MPa and room temperature have useable volumetric and gravimetric storage capacities of 0.0244 kg H_2/L and 4.2 wt %, respectively [4], below the DOE 2025 targets. Hydrogen storage on solid porous materials is a promising method to reach the mentioned target. The hydrogen gas is stored by physisorption on the pores of these materials. One advantage of this storage method is that the storage of hydrogen gas on solid porous materials achieves higher densities at low and moderate pressures than the compression storage method at the same pressures. The storage at low and moderate pressure is cheaper than at high pressures.

Another way to reduce CO_2 emissions is through road transport based on NGVs, which are less polluting than oil-based vehicles. They emit much less CO_2 and they could be a key element to reach the emission goals of the European Union, 95 g of CO_2/km. Most of Natural Gas Vehicles are Compressed Natural Gas (CNG) vehicles. They store natural gas (most of natural gas is composed by methane) by compression up to 25, 35 or 70 MPa and have an autonomy of about 600 km. Adsorbed Natural Gas (ANG) vehicles, store methane (natural gas) on deposits that contain an adsorbent material, a solid porous material. This storage method has the same advantage that the storage of hydrogen on porous solid materials. The technological goal is an ANG vehicle that works at low or moderate pressures, with the same autonomy range than a CNG vehicle that works at high pressures. The U.S. DOE established the following on-board useable methane storage targets at room temperature and moderate pressures (6–25 MPa) to reach that technological goal: 0.250 kg CH_4/L and 33.33 wt % for the useable volumetric and gravimetric storage capacities, respectively [5].

The research on the field of gas storage on solid porous materials is focused on the search of materials that can be used at room temperature and that store enough gas to be used in the deposits of a hydrogen vehicle [6,7] or an ANG vehicle. There are several classes of solid porous materials used for gas storage. Among them, nanoporous activated carbons (ACs) have been extensively studied for their exceptional gas storage capacities [8–13]. These materials exhibit a well-developed porosity, providing ample space for gas molecules to be stored, and they are relatively non-expensive to synthesize. Polymer composites, which consist of a polymer matrix reinforced with porous fillers, offer a unique combination of mechanical strength and gas storage capabilities [14,15]. Composites made with inexpensive polymers like polypropylene or polyester and low-cost fillers such as glass fibers can be relatively affordable. Polymers of Intrinsic Microporosity (PIMs) are an intriguing class of porous materials that have garnered significant attention in gas storage applications. PIMs possess a molecular structure that inherently incorporates microporosity, resulting in materials with exceptionally high internal surface areas. This characteristic allows PIMs to exhibit enhanced gas sorption capacities [6,16]. Covalent organic frameworks (COFs) are a class of porous materials constructed through covalent bonding of organic building blocks. COFs exhibit permanent porosity and tunable structures, making them attractive for gas storage applications [17,18].

Metal-Organic Frameworks (MOFs) are a significant and large class of porous materials that have gained considerable attention in gas storage applications. MOFs consist of metal nodes or clusters connected by organic ligands, forming highly ordered crystalline structures with well-defined pores. The tunable nature of MOFs allows for precise control over their porosity and gas adsorption properties. As a result, MOFs have shown great potential for various gas storage applications. There is very intense research related to these materials: There were over 90,000 MOFs synthesized and 900,000 MOF structures predicted by August 2020 [19]. The hydrogen and methane storage capacities of MOFs have been extensively studied in experiments and GCMC simulations [20–36]. The high porosity of MOFs and their high surface area to volume ratio make them promising candidates for on-board hydrogen and methane storage. However, the synthesis of most MOFs is very expensive [28].

Recently, a group of the Beijing University of Technology has published the synthesis of a new group of BUT MOFs using materials and a method that reduces the cost [37]. GCMC simulations were conducted to predict and understand the hydrogen and methane storage capacities of these new BUTs at room temperature and pressures ranging from 0.5 to 50 MPa. The paper is organized as follows. Section II is devoted to the details of the GCMC simulations and of the BUT cells. The results of the simulations are presented and analyzed in section III. Finally, section IV is devoted to the conclusions.

Methodology and materials simulated

Parameters and details of the GCMC simulations

GCMC simulations of hydrogen and methane molecules inside the eleven BUTs recently synthesized [37] have been carried

out at room temperature, 298.15 K, and at pressures between 0.5 and 35 MPa. A few simulations have been also carried out at 50 MPa for some selected BUTs. Each GCMC simulation consisted of ten million iterations. The storage capacities were calculated using the last five million iterations of each simulation. The Metropolis algorithm was used in each iteration [38]. On each iteration there are three possible trials: Move, add or remove one molecule. 40% of the trials consisted on the deletion of one molecule, another 40% on the insertion of one molecule and the remaining 20% consisted on the movement of one molecule. These percentages of the trials were obtained after several test simulations. The simulations have been performed using an in-house code.

The chemical potential used in the GCMC simulations was derived from the Soave-Redlich-Kwong (SRK) [39] equation of state (EOS), using for the dimensionless acentric factor ω, the critical pressure P_c and the critical temperature T_c of hydrogen and methane, the values published by Zhou and Zhou [40] and Xu et al. [41], respectively (See Table 1).

The Lennard-Jones (LJ) interaction potential energy [42] has been used to simulate the interactions between the gas (hydrogen or methane) molecules and between the gas molecules and the atoms of the BUTs. The LJ interaction potential energy has the form:

$$V = 4\varepsilon\left[\left(\frac{\sigma}{r}\right)^{12} - \left(\frac{\sigma}{r}\right)^{6}\right], \tag{1}$$

where -ε is the minimum value of the LJ interaction potential energy ($\varepsilon > 0$), σ is the distance at which the interaction between the two particles is zero and r is the distance between the two particles. The values of the parameters σ and ε depend on the particles of the interaction. The σ and ε parameters of the interaction between atom i and gas j were obtained through the Good-Hope [43] and Berthelot combining rules [44], respectively:

$$\begin{aligned}\sigma_{ij} &= \sqrt{\sigma_i \sigma_j}\\ \varepsilon_{ij} &= \sqrt{\varepsilon_i \varepsilon_j}.\end{aligned} \tag{2}$$

Table 2 shows the values of the LJ parameters ε and σ of the atoms and molecules used in the present GCMC simulations of the BUTs. The LJ parameters of the C–H_2 interaction used in the simulations were obtained from Rzepka et al. [45]. The LJ parameters of the rest of the interactions were obtained by means of the above-mentioned Good-Hope-Berthelot combining rule. The quantum effects have been included in the interaction potential by using the Feynman-Hibbs correction [46]. All the present GCMC simulations have been performed using that quantum correction.

The LJ interaction potential was cut off at 20 Å for the interactions with H_2 and at 7.5 Å for the interactions with methane. These values of the cutoff radii were obtained after carrying out two sets of GCMC simulation tests of pure hydrogen and methane in a simulation box of 50 × 50 × 50 $Å^3$ at 298.15 K and at several values of the 'experimental' or input pressure, between 0.1 and 25 MPa for hydrogen and between 0.1 and 35 MPa for methane. The goal of those tests was the calculation of the density and the pressure of the gas.

Table 1 – Parameters of the SRK equation of state of hydrogen and methane: ω, P_c in MPa and T_c in K.

Gas	ω	P_c	T_c	Source
H_2	−0.216	1.28	33.2	[40]
CH_4	0.01142	4.5992	190.56	[41]

The first set of tests consisted on the comparison of the SRK EOS density and the density obtained in the GCMC simulations at 298.15 K. Fig. 1 contains this comparison for hydrogen and methane. There is a good agreement between these two densities for hydrogen and methane using the mentioned values of the cutoff radii. The present tests for H_2 were previously published and were performed using the same LJ parameters [59].

The second tests consisted on the comparison of the input pressure and the pressure calculated in the GCMC simulations at 298.15 K. The input pressures were in the range 0.5–25 MPa for hydrogen and in the range 0.5–35 MPa for methane. The calculated pressure, P_{calc}, was computed by means of [60,61]:

$$P_{calc} = \frac{N k_B T}{V} - \frac{2\pi N^2}{3V^2}\int_0^\infty r^3 U(r) g(r) dr, \tag{3}$$

where N, T and V are the average number of H_2 or CH_4 molecules, the temperature and the volume of the simulation box, respectively. k_B is the Boltzmann constant, $U(r)$ is the LJ interaction potential between the molecules and $g(r)$ is the pair distribution function. That function was calculated from the positions of the molecules obtained in 50,000 configurations on each simulation. The comparisons of the input and calculated pressures for hydrogen and methane are plotted in Fig. 2. There is a good agreement between these two pressures for both gases.

Definitions of the storage capacities

The total (hydrogen or methane) volumetric and gravimetric storage capacities have been calculated in the GCMC simulations, according to the following definitions. The total (hydrogen or methane) volumetric storage capacity, v_c, also called the density of stored (hydrogen or methane), is defined by

$$v_c = \frac{M_g}{V}, \tag{4}$$

where V is the volume of the simulation cell and M_g is the mass of gas (hydrogen or methane) stored in the simulation cell. Throughout this paper, v_c is calculated in kg of gas (H_2 or CH_4)/L units. The other storage capacity obtained in the simulations is the total (hydrogen or methane) gravimetric storage capacity, g_c, which is defined by

$$g_c = \frac{100 M_g}{M_g + M_{ads}}, \tag{5}$$

where M_{ads} is the mass of the adsorbent solid porous material of the simulation cell. According to this definition, the total gravimetric capacity is calculated in wt. % units.

The definition of the useable (hydrogen or methane) storage capacities is related to the total storage capacities. The useable mass of gas (hydrogen or methane) stored at a given pressure P and temperature T is the difference between the

Table 2 – LJ parameters of the atoms and molecules used in the GCMC simulations. σ is in Å and ε in eV.

	σ	ε	Source		σ	ε	Source
B	3.453	0.004116	[47]	H_2	2.970	0.002870	[45]
C	3.400	0.003744	[48]	In	2.810	0.052290	[49]
Cd	2.700	0.000259	[50]	Mn	2.587	0.047219	[51]
Cu	2.297	0.520310	[52]	N	3.310	0.003214	[53]
CH_4	3.730	0.012748	[54]	O	3.033	0.004150	[55]
Hf	2.798	0.003122	[56]	Zn	0.998	0.008291	[57]
H	2.846	0.000659	[55]	Zr	2.910	0.735981	[58]
C–H_2	3.190	0.002628	[45]				

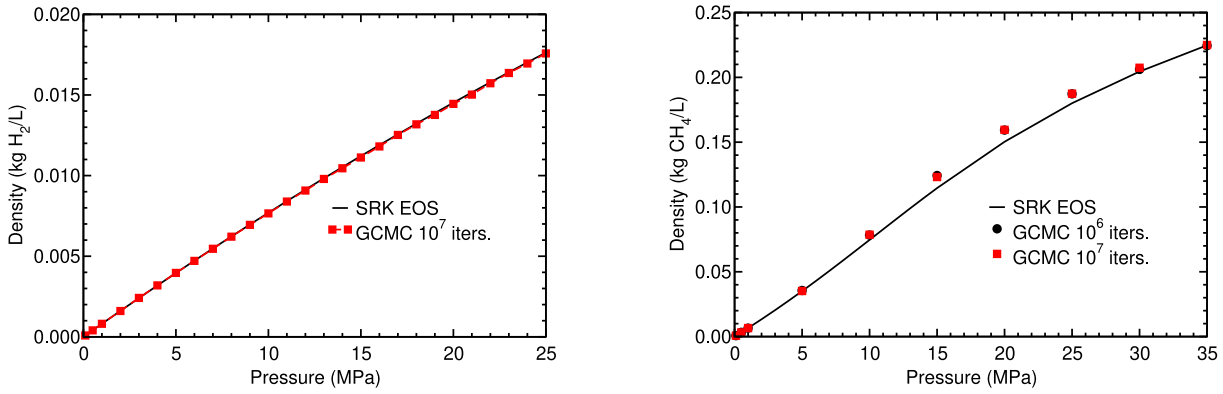

Fig. 1 – SRK EOS density and GCMC density vs pressure obtained in the simulations of one and ten million of iterations of pure H_2 (left panel) and CH_4 (right panel) vs pressure at 298.15 K.

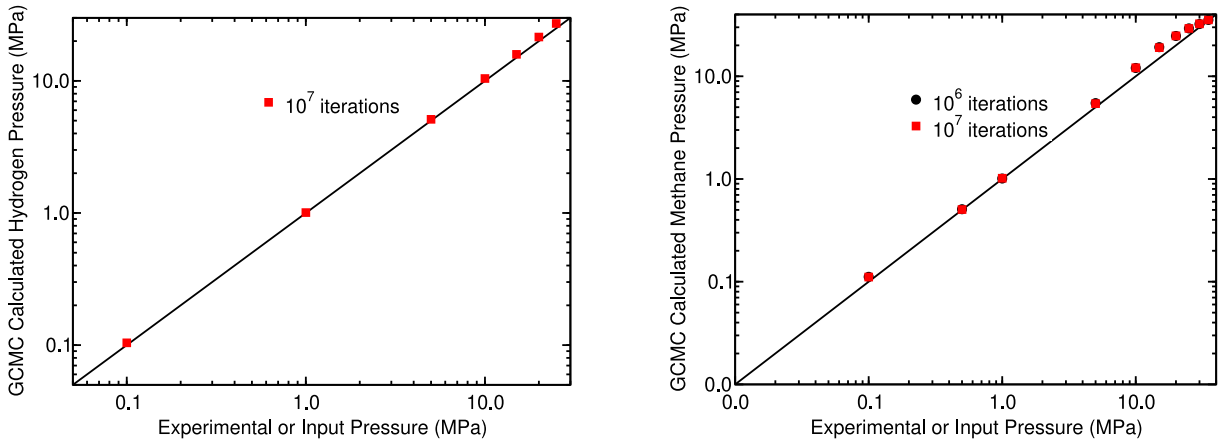

Fig. 2 – GCMC calculated pressure vs the 'experimental' or input pressure, obtained in the simulations of one and ten million of iterations of H_2 (left panel) and CH_4 (right panel) at 298.15 K.

total mass of gas stored at that P and T and the total mass of gas stored at the depletion (also called minimum or back) pressure and T [3,62–64]. The useable (hydrogen or methane) volumetric and gravimetric capacities are calculated inserting in Eqs. (4) and (5) the useable mass of gas stored. Throughout this paper, the focus will solely be on total and useable storage capacities.

Simulation cells of the BUTs

The simulation cells of the new BUTs (See Fig. 3) were obtained from the data in Crystallographic Information File (CIF) format reported by Kong et al. [37]. These CIF files were retrieved from the Cambridge Crystallographic Data Centre, CCDC [65]. There are eleven new BUTs: BUT-101(Zn), BUT-

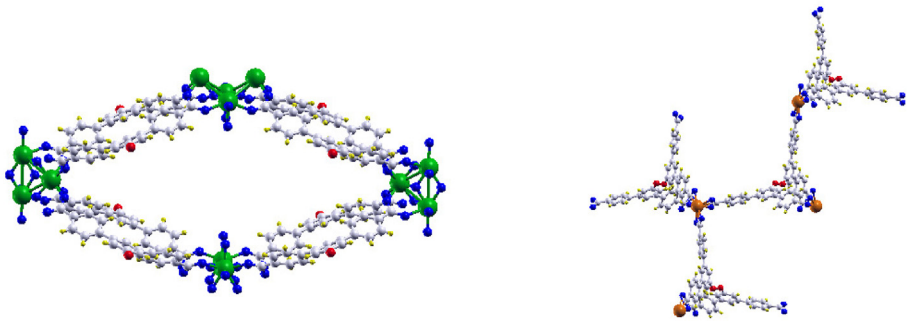

Fig. 3 – Simulation cell of BUT-104 (left panel) and BUT-107 (right panel). Oxygen, nitrogen, carbon, hydrogen, zirconium and indium atoms are represented by blue, red, gray, yellow, green and orange balls, respectively. (For interpretation of the references to color in this figure legend, the reader is referred to the Web version of this article.)

101(Cu), BUT-102, BUT-103, BUT-104, BUT-105, BUT-106, BUT-107, BUT-108(Hf), BUT-108(Zr) and BUT-109(Zr). The CCDC numbers of this group of BUTs are 1888829–1888839. The volume of the simulation cells of these eleven BUTs is in the range 9300–28000 $Å^3$, except the volume of the BUT-105 cell, which is much larger, about 108,000 $Å^3$.

Calculation of the porosity

The porosity is calculated as the ratio of the available volume and the volume of the simulation cell of a MOF. It is a dimensionless magnitude. The available volume to a gas molecule is the difference between the volume of the simulation cell, *V*, and the volume occupied by the atoms of the MOF, V_{occ}.

The volume V_{occ} is calculated approximately as follows: A grid of *n* points contained in the simulation cell is created. *ni* is the number of grid points that are inside the sphere of some atom of the simulation cell. The volume V_{occ} is given by the *Vni/n*. The volume of the sphere of an atom is given by $4\pi r^3/3$, where *r* is the radius of the atom and is equal to σ(atom, molecule). The LJ interaction potential energy is zero at an atom-molecule distance equal to σ(atom, molecule). Due to this definition of the radius of an atom interacting with a molecule, the volume occupied by the atoms, the available volume and the porosity depend on the type of gas molecule. The porosity measured in the experiments also depends on the type of gas.

Calculation of the pore size

The BUTs were analyzed using an algorithm to determine the presence of pores with a radius equal to or greater than 3 Å. Pores with a smaller radius cannot accommodate hydrogen and methane molecules. The algorithm begins by generating a three-dimensional grid of points within the BUT cell. The grid points are spaced at a distance of 1.0 Å. In the next step, for each grid point *i*, the algorithm calculates the distance d_{ij} from point *i* to each atom *j* in the cell. The minimum distance, denoted as *dmin*(*i*), is then determined for each grid point. This process is repeated for all grid points *i*.

In the third step, the algorithm calculates the pore radius as follows: the largest value among all *dmin*(*i*) is considered the radius of a pore, with the corresponding grid point *i* serving as the center of the pore. The set of *dmin*(*i*) values is then recalculated. The grid points contained within this new pore are treated as 'atoms' within the BUT structure, and the second step is repeated to obtain a new set of *dmin*(*i*) values. This process continues until the largest value among all *dmin*(*i*) values is smaller than 3 Å. The algorithm yields a collection of pore radii, along with the average pore radius. The initial pore radius obtained using this algorithm corresponds to the largest pore radius found. It is important to note that the spherical pores obtained using this algorithm do not overlap.

Results and discussion

GCMC hydrogen storage capacities of BUTs

Hydrogen storage capacities vs porosity, density and pore size

The useable capacities of the eleven novel BUTs obtained in the GCMC simulations at 298.15 K and 25 MPa are tabulated in Table 3 and plotted in Fig. 4, as functions of the porosity, density and largest pore radius of the BUTs. Eight of the new BUTs have volumetric capacities in the range of 0.011–0.016 kg/L and gravimetric capacities above 1 wt % at 298.15 K and 25 MPa (See Table 3). The remaining three BUTs (102, 103 and 106) have volumetric capacities below 0.008 kg/L and gravimetric capacities below 0.5 wt %. BUT-104, 105 and 107 have the largest storage capacities. These three BUTs have been selected to make more simulations and further analysis in another subsection.

The analysis of the dependence on those variables shows that there are approximate correlations between the storage capacities and the porosity and density: a) The smaller the density, the larger the storage capacities, b) The larger the porosity, the larger the storage capacities, and c) The BUTs with the highest capacities have porosities above 0.4 and densities smaller than 0.6 kg/L. These are approximate correlations, because not all the capacities of the BUTs follow exactly these correlations.

Table 3 – Useable hydrogen storage capacities and isosteric heat at room temperature and 25 MPa of the new BUTs. The porosity is dimensionless. The density, the largest pore radius, the average pore radius, the isosteric heat, v_c and g_c are in kg/L, Å, Å, eV, kg of H_2/L and wt. %, respectively. R stands for pore radius.

BUT	porosity	density	largest R	average R	Q_{st}	v_c	g_c
101(Cu)	0.214	0.967	6.95	6.82	0.072	0.0138	1.41
101(Zn)	0.207	0.995	6.74	6.55	0.066	0.0114	1.13
102	0.106	1.592	4.73	3.92	0.067	0.0078	0.49
103	0.025	1.299	4.15	3.46	0.076	0.0035	0.27
104	0.416	0.596	7.57	7.44	0.051	0.0159	2.60
105	0.539	0.496	12.66	7.35	0.039	0.0139	2.73
106	0.061	1.323	4.39	3.71	0.066	0.0066	0.49
107	0.680	0.286	8.80	6.89	0.038	0.0161	5.32
108(Hf)	0.308	1.250	6.84	4.40	0.055	0.0129	1.02
108(Zr)	0.310	0.966	6.88	4.81	0.063	0.0155	1.58
109(Zr)	0.328	0.859	8.43	7.74	0.059	0.0135	1.55

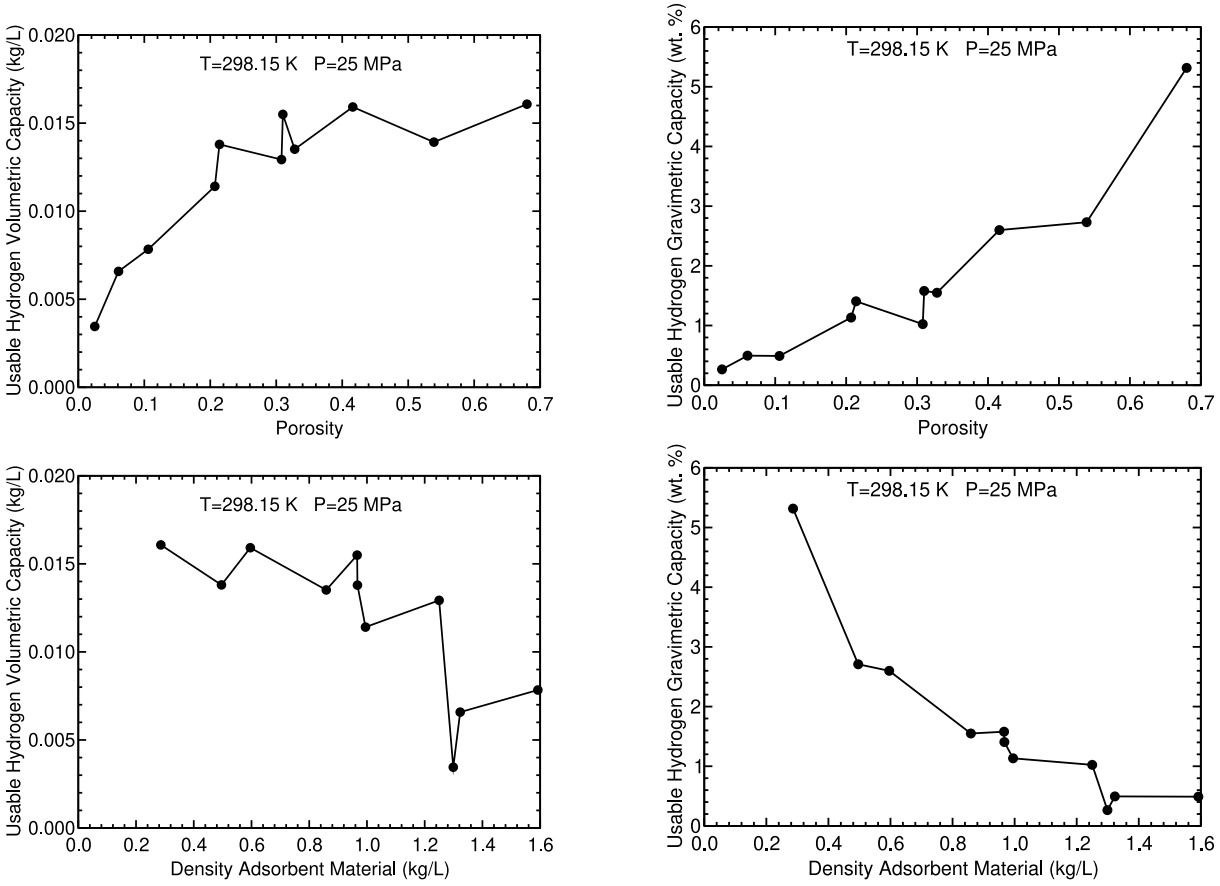

Fig. 4 – Useable hydrogen volumetric and gravimetric capacities of BUTs at room temperature and 25 MPa vs their porosities (upper panels) and densities (lower panels).

Another important structural factor of the BUTs is the pore size. The largest and average pore radius of the BUTs have been calculated. The dependence of the useable v_c and g_c on the largest and average pore radius can be noticed in Fig. 5. The volumetric capacity increases rapidly as the (largest or average) radius R increases and then reaches a constant value. Wide pores can not contain or store more gas molecules and this explains the trend towards a constant value.

In contrast, the gravimetric capacity increases linearly with the (largest or average) radius R, if the g_c corresponding to BUT-107, which is an outlier, is not considered. The gravimetric capacity of BUT-107 is very high due to its low density, 0.286 kg/L (See Table 3). That linear increase can be explained as follows: As the pore radius increases, the BUTs are, in general, lighter and hence, the gravimetric capacity increases.

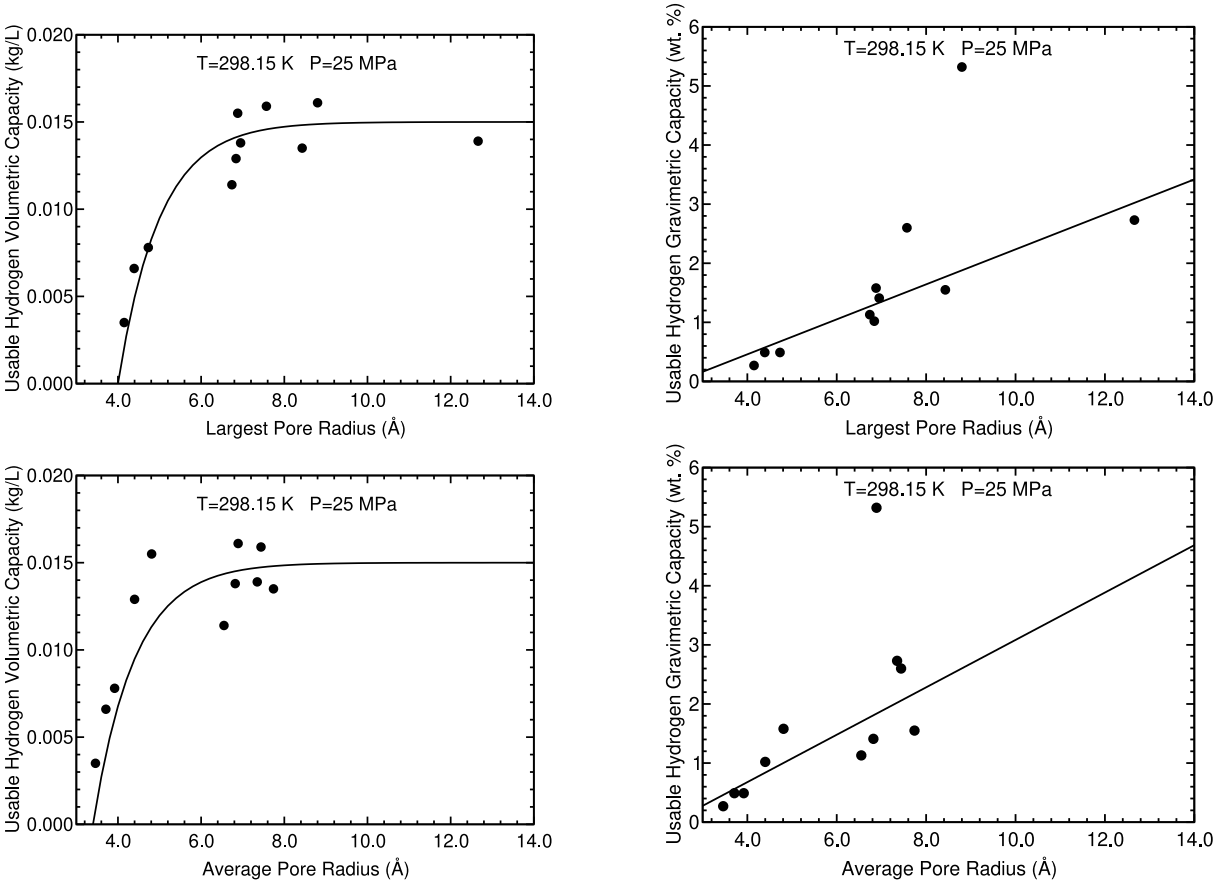

Fig. 5 – Useable hydrogen volumetric and gravimetric capacities of BUTs at room temperature and 25 MPa vs their largest pore radius (upper panels) and average pore radius (lower panels).

Table 4 – Hydrogen isosteric heat (in eV) of several solid porous materials. Temperature is in K.

Material	Q_{st}	Temperature	Source
Zeolites	0.21–0.83	279–323	[72,73]
Activated carbons	0.06–0.11	298.15	[74,75]
MOFs	0.04–0.33	298–300	[33,66,67]
BUTs	0.038–0.076	298.15	Present work

Isosteric heat of hydrogen adsorption

The isosteric heat, Q_{st}, of hydrogen adsorption of MOFs at room temperature is usually in the range 0.04–0.07 eV [33] (See Table 4). Recently, a research group measured the isosteric heat of hydrogen adsorption of a Vanadium-based MOF and obtained a value of 0.217 ± 0.002 eV [66]. The highest isosteric heat among the MOFs corresponds to Cu^{I}-MFU-4L (Multi-Functionalized): 0.33 eV [67]. These isosteric heats can be compared with those of activated carbons, which have hydrogen isosteric heats at room temperature in the range of 0.06–0.11 eV (See Table 4).

Different theoretical approaches [68–70] showed that the isosteric heat of adsorption should be about 0.1–0.3 eV in order to reach the DOE hydrogen storage targets and a reversible storage at room temperature and moderate pressures. Bae and Snurr [71] studied eight MOFs at 298 K and pressures between 0.15 and 12 MPa and found that the optimal isosteric heat was between 0.19 and 0.23 eV.

The isosteric heat of hydrogen adsorption of the novel BUTs obtained in the present GCMC simulations at 298.15 K and 25 MPa lies in the range 0.038–0.076 eV (See Tables 3 and 4), within the usual range of values for MOFs, and smaller than the isosteric heats of zeolites. According to the mentioned theoretical approaches, these values seem to be low and below the estimated isosteric heat necessary to reach the DOE hydrogen targets. However, according to the GCMC simulations, the storage capacities of some BUTs are relatively high, even close to some DOE 2025 target.

The mentioned theoretical approaches indicate that the lower the isosteric heat, the lower the capacities. A plot of the useable hydrogen capacities of all the novel BUTs vs the isosteric heat at 298.15 and 25 MPa in Fig. 6 shows that there is not a clear correlation between the useable hydrogen v_c and the isosteric heat. The useable g_c seems to decrease as the isosteric heat increases. BUT-107 has the highest useable v_c and g_c, 0.016 kg/L and 5.32 wt %, respectively, and also has the lowest isosteric heat, 0.038 eV, among the novel BUTs at 298.15 and 25 MPa.

These GCMC results do not coincide with the theoretical approaches. Some authors have argued that, besides of a large isosteric heat, a large porosity, especially at pressures larger than approximately 5–7 MPa, is also necessary to

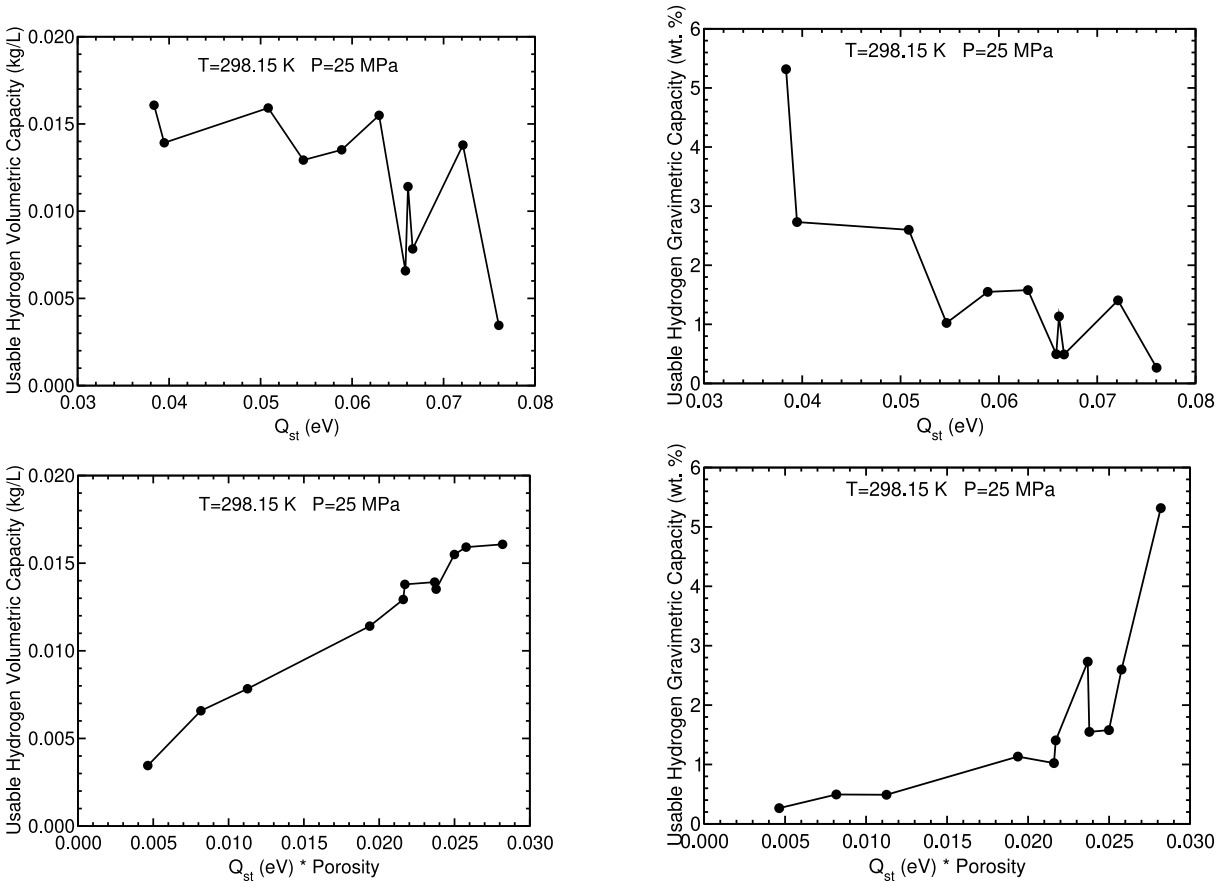

Fig. 6 – Useable hydrogen volumetric and gravimetric capacities vs isosteric heat (upper panels) and vs isosteric heat multiplied by porosity (lower panels) at room temperature and 25 MPa of the novel BUTs.

reach the DOE hydrogen targets [30]. Frost and Snurr showed that MOFs with larger porosities provide, in general, lower isosteric heats [76]. That general correlation also exists in BUTs: BUT-104, 105 and 107 have the highest storage capacities, the highest porosities and the lowest isosteric heats (See Table 3).

In order to understand the storage capacities, the isosteric heat and the porosity must be considered. The storage capacities have been plotted as a function of the product of the isosteric heat and the porosity at 298.15 K and 25 MPa in Fig. 6. The v_c is approximately correlated with that product: The volumetric capacity increases as the product increases, in general. The g_c also increases, in general, with the product, although the correlation is less clear than in the case of the volumetric capacity. These results indicate that both, the isosteric heat and the porosity, play a role in the storage capacities.

The useable hydrogen gravimetric capacity has a much better correlation with Q_{st} if the density of the adsorbent material, ρ_{ads}, is also considered as follows. The gravimetric capacity is given by Eq. (5). The mass of the adsorbent material is equal to $\rho_{ads}V$, where V is the volume of the cell containing the material. The mass of gas is given by v_cV. Therefore, Eq. (5) can be also written as

$$g_c = \frac{100 v_c}{v_c + \rho_{ads}}. \quad (6)$$

The useable hydrogen volumetric capacity is much smaller than ρ_{ads} and hence, Eq. (6) can be approximated by

$$g_c \approx \frac{100 v_c}{\rho_{ads}}. \quad (7)$$

According to Eq. (7) g_c is inversely proportional to the density of the adsorbent material. Therefore, it makes sense to analyze g_c as a function of Q_{st}/ρ_{ads} and Q_{st}/ρ_{ads} Porosity. Fig. 7 contains the plots of g_c vs those two variables. The g_c is approximately proportional to Q_{st}/ρ_{ads}, but there is not a clear correlation at low values of Q_{st}/ρ_{ads}. On the other hand, there is a very good correlation between g_c and the product of porosity and Q_{st}/ρ_{ads}, much better than between g_c and Q_{st}/ρ_{ads} (Compare Figs. 6 and 7).

The dependence of the isosteric heat of the BUTs on the largest and average pore radius is plotted in Fig. 8. It can be noticed in that figure that the isosteric heat has not a clear dependence on the average pore radius: All the isosteric heat points are concentrated in a short region of the isosteric heat-average pore radius plot. On the other hand, there is a dependence on the largest pore radius: The isosteric heat, in

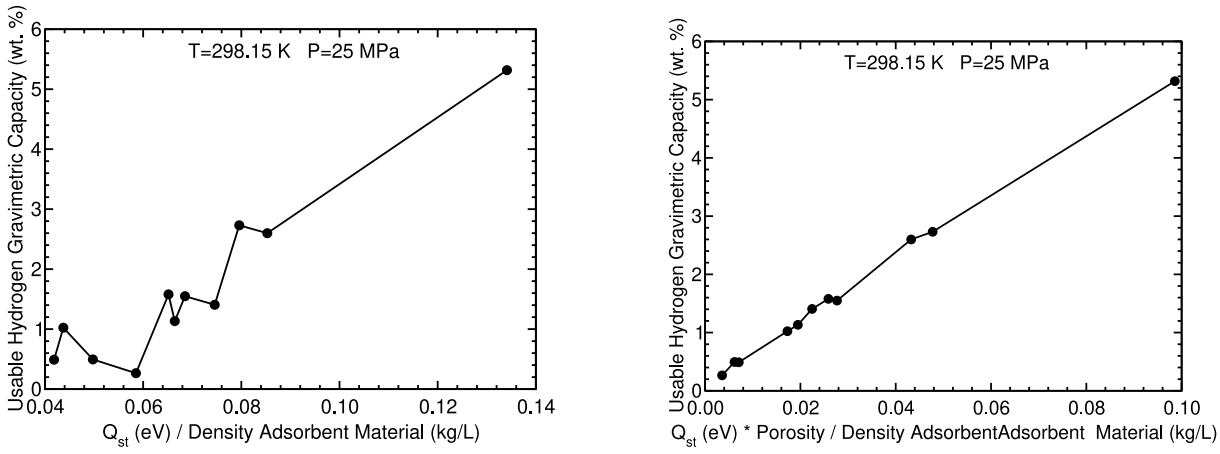

Fig. 7 – Useable hydrogen gravimetric capacities vs Q_{st}/ρ_{ads} vs Q_{st}/ρ_{ads} multiplied by porosity at room temperature and 25 MPa of the novel BUTs.

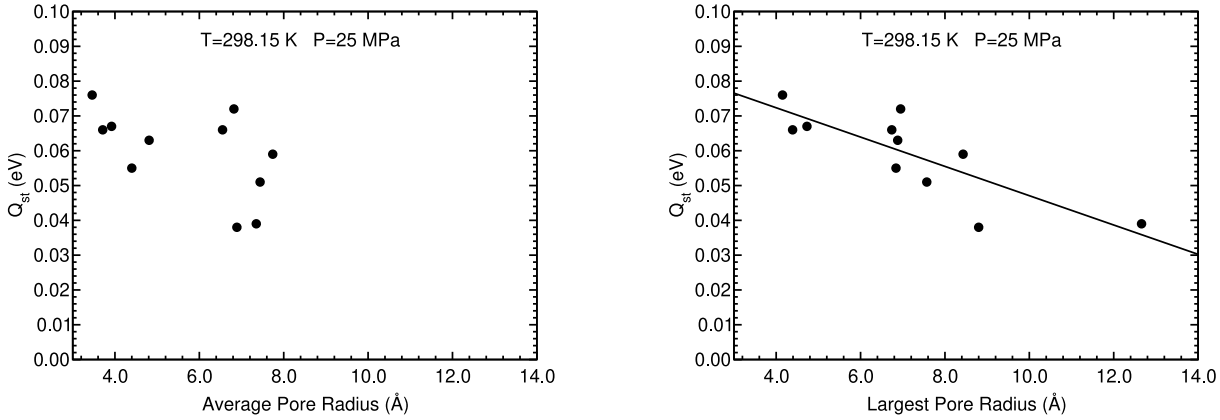

Fig. 8 – Hydrogen isosteric heat (in eV) at 25 MPa and 298.15 K vs the average and largest pore radius (in Å) of the novel BUTs.

general, decreases linearly as the largest pore radius increases.

Hydrogen storage capacities vs pressure

The total and useable storage capacities at 298.15 K of the three selected BUTs (104, 105 and 107) are plotted in Fig. 9, respectively, as a function of the pressure between 0.5 and 50 MPa. These are the so-called isotherms and can be compared with experiments and theoretical results (See Table 5).

The total hydrogen volumetric storage capacities of carbon slit pores and nanotubes of pore width or diameter of 7–15 Å are between 0.016 and 0.022 kg/L at 25 MPa and 298.15 K, according to previous GCMC simulations [59]. The total hydrogen volumetric capacities of the three BUTs at 25 MPa and 298.15 K are between 0.0142 and 0.0166 kg/L, slightly lower than the total volumetric capacities of the above-mentioned carbon nanostructures. Rzepka et al. [45] obtained in GCMC simulations of carbon-based slit pores a volumetric capacity of 0.0235 kg/L at 30 MPa and 300 K for a pore width of 7 Å. The total volumetric capacities of the three BUTs at 298.15 K and 30 MPa are between 0.0165 and 0.0192 kg/L. Hence, these BUTs have slightly lower volumetric capacities than carbon-based slit pores.

Kunowsky et al. made hydrogen storage experiments of a large range of KOH activated carbon fibres (ACFs) and obtained that the maximum total volumetric capacity of the ACFs at 298 K and 20 MPa was 0.0171 kg/L [77]. At 298.15 K and 20 MPa, the total hydrogen volumetric capacities of the three BUTs are between 0.012 and 0.014 kg/L, about a 20–30% smaller than the total volumetric capacities of ACFs. The volumetric capacities of MOFs at room temperature and 5–10 MPa are between 0.0005 and 0.0150 kg/L [30]. The volumetric capacities of the three BUTs at 298.15 K and 10 MPa are between and 0.0066 and 0.0080 kg/L, within the above-mentioned range of values.

The useable hydrogen volumetric storage capacities of these three BUTs at 298.15 K and 25–35 MPa are high and between 0.014 and 0.021 kg/L. At 50 MPa and 298.15 K, the useable hydrogen volumetric capacities of the three BUTs are between 0.023 and 0.027 kg/L, close to the DOE 2020 target, 0.030 kg/L, but they are about a 30–60% below the DOE 2025 target, 0.040 kg/L.

As regards gravimetric capacities, the total gravimetric capacities of the BUTs 104, 105 and 107 are 2.70, 2.78 and

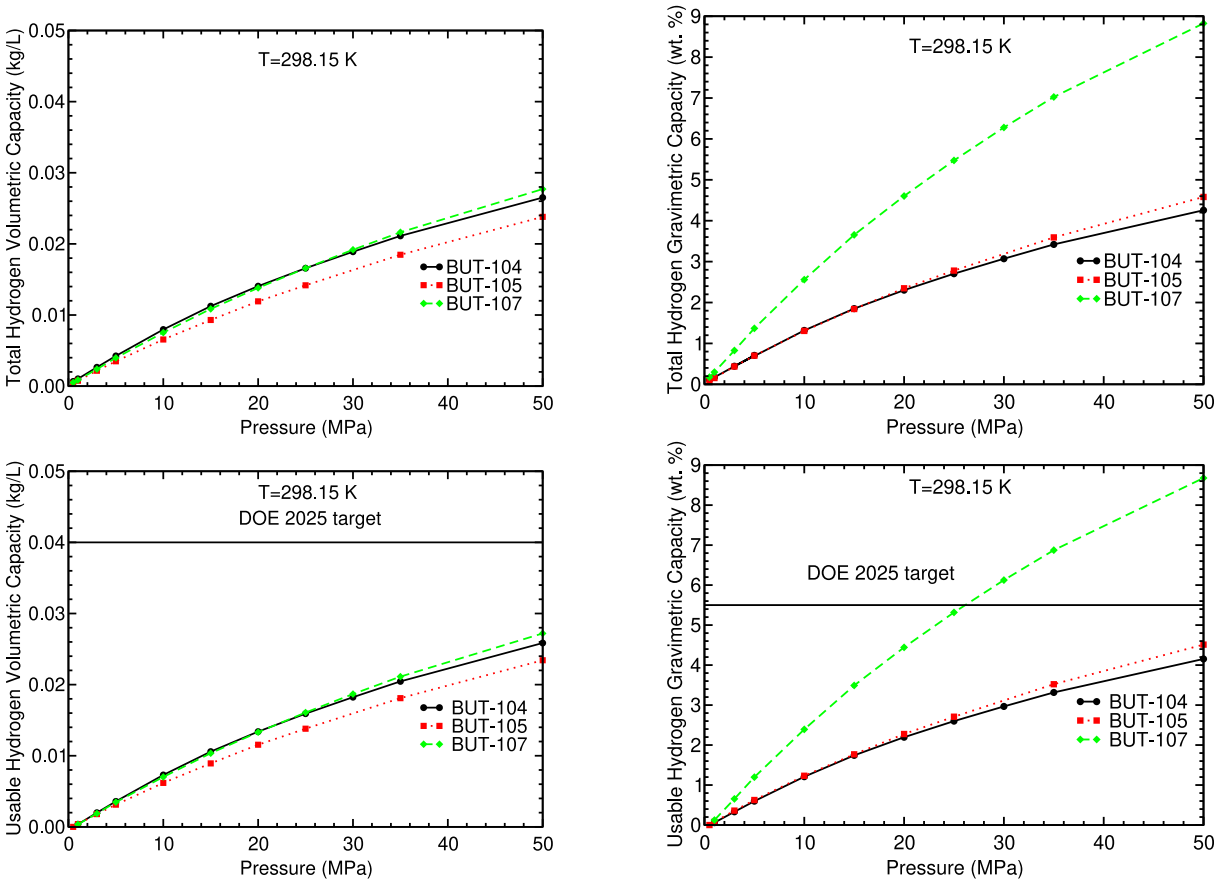

Fig. 9 – Total (upper panels) and useable (lower panels) hydrogen volumetric and gravimetric capacities vs pressure at room temperature of three selected BUTs.

Table 5 – Total hydrogen volumetric (in kg/L) and gravimetric (in wt. %) storage capacities of several solid porous materials. Temperature and pressure are in K and MPa, respectively.

Material	v_c	g_c	T	P	Source
Carbon nanostructures	–	0.7	303	10	[78]
Carbon nanostructures	–	0.1–1.6	296.15	10	[79]
Slit Pore 7 Å	0.0235	0.95	300	30	[45]
BUT-104, 105 and 107	0.0165–0.0192	3.07–6.28	298.15	30	Present work
Slit Pores 7–15 Å	0.016–0.022	0.9–1.8	298.15	25	[59]
Nanotubes 7–15 Å	0.016–0.022	0.4–0.9	298.15	25	[59]
BUT-104, 105 and 107	0.0142–0.0166	2.70–5.47	298.15	25	Present work
ACFs	0.0171	1.3	298	20	[77]
MOFs	0.0005–0.0150	–	RT	5–10	[30]
MOFs	–	0.3–2.3	RT	6–10	[30]
MOFs	–	0.4–4	RT	8,10	[33]
BUT-104, 105 and 107	0.0066–0.0080	1.32–2.56	298.15	10	Present work

5.47 wt %, respectively, at 298.15 K and 25 MPa. These gravimetric capacities are much larger than the total hydrogen gravimetric capacities of carbon slit pores and nanotubes of width or diameter in the range 7–15 Å, obtained in previous GCMC simulations at the same temperature and pressure [59]: The total capacities of slit pores and nanotubes are in the ranges 0.9–1.8 wt % and 0.4–0.9 wt %, respectively. The total gravimetric capacities at 30 MPa of the three BUTs (104, 105 and 107) are 3.07, 3.23 and 6.28 wt %, respectively, much larger than the capacity of 0.95 wt % obtained by Rzepka et al. [45] in GCMC simulations at 30 MPa and 300 K for a pore width of 7 Å.

The total gravimetric capacities of the BUTs 104, 105 and 107 at 298.15 K and 10 MPa are 1.32, 1.31 and 2.56, respectively. These capacities are similar or larger than those of activated carbons at room temperature and 10 MPa. Experiments performed by Xu et al. [78] on various carbon materials (activated

Table 6 – Useable methane storage capacities and isosteric heat at room temperature and 25 MPa of the new BUTs. The porosity is dimensionless. The density, the largest pore radius, the average pore radius, the isosteric heat, v_c and g_c are in kg/L, Å, Å, eV, kg of H_2/L and wt. %, respectively. R stands for pore radius.

BUT	porosity	density	largest R	average R	Q_{st}	v_c	g_c
101(Cu)	0.153	0.967	6.95	6.59	0.208	0.1104	10.25
101(Zn)	0.146	0.995	6.74	6.43	0.198	0.1144	10.31
102	0.066	1.592	4.75	3.90	0.187	0.0528	3.21
103	0.010	1.299	4.03	3.43	0.192	0.0365	2.73
104	0.338	0.596	7.57	7.36	0.180	0.1960	24.73
105	0.486	0.496	12.64	4.76	0.112	0.1619	24.62
106	0.029	1.323	4.35	3.64	0.187	0.0685	4.92
107	0.630	0.286	8.80	6.19	0.132	0.2104	42.35
108(Hf)	0.240	1.250	6.70	4.29	0.157	0.1365	9.84
108(Zr)	0.243	0.966	6.74	4.55	0.177	0.1302	11.88
109(Zr)	0.274	0.859	8.43	7.74	0.160	0.1341	13.50

carbon, single-walled carbon nanohorn, single-walled carbon nanotubes, and graphitic carbon nanofibers) showed that the gravimetric capacity of these materials is less than 0.7 wt % at 303 K and 10 MPa. Ströbel et al. reported the results of hydrogen storage experiments on a variety of carbon nanostructures [79]. They obtained gravimetric capacities at 296.15 K and 10 MPa between 0.1 and 1.6 wt %.

At 298.15 K and 20 MPa, the total gravimetric capacities of the BUTs 104, 105 and 107 are 2.30, 2.35 and 4.60 wt %, respectively. These gravimetric capacities are also larger than the capacities of activated carbons at room temperature and 20 MPa. Kunowsky et al. [77] obtained that the maximum excess gravimetric capacity of a large range of ACFs at 298 K and 20 MPa was 1.1 wt % (the total gravimetric capacity could be estimated to be about 1.3 wt %).

According to a review by Langmi et al. [30] of the hydrogen storage capacities of MOFs, the gravimetric capacities of MOFs at room temperature and pressures of 6–10 MPa are in the range 0.3–2.3 wt %. Experiments on MOFs showed that the H_2 gravimetric storage capacities of MOFs at room temperature

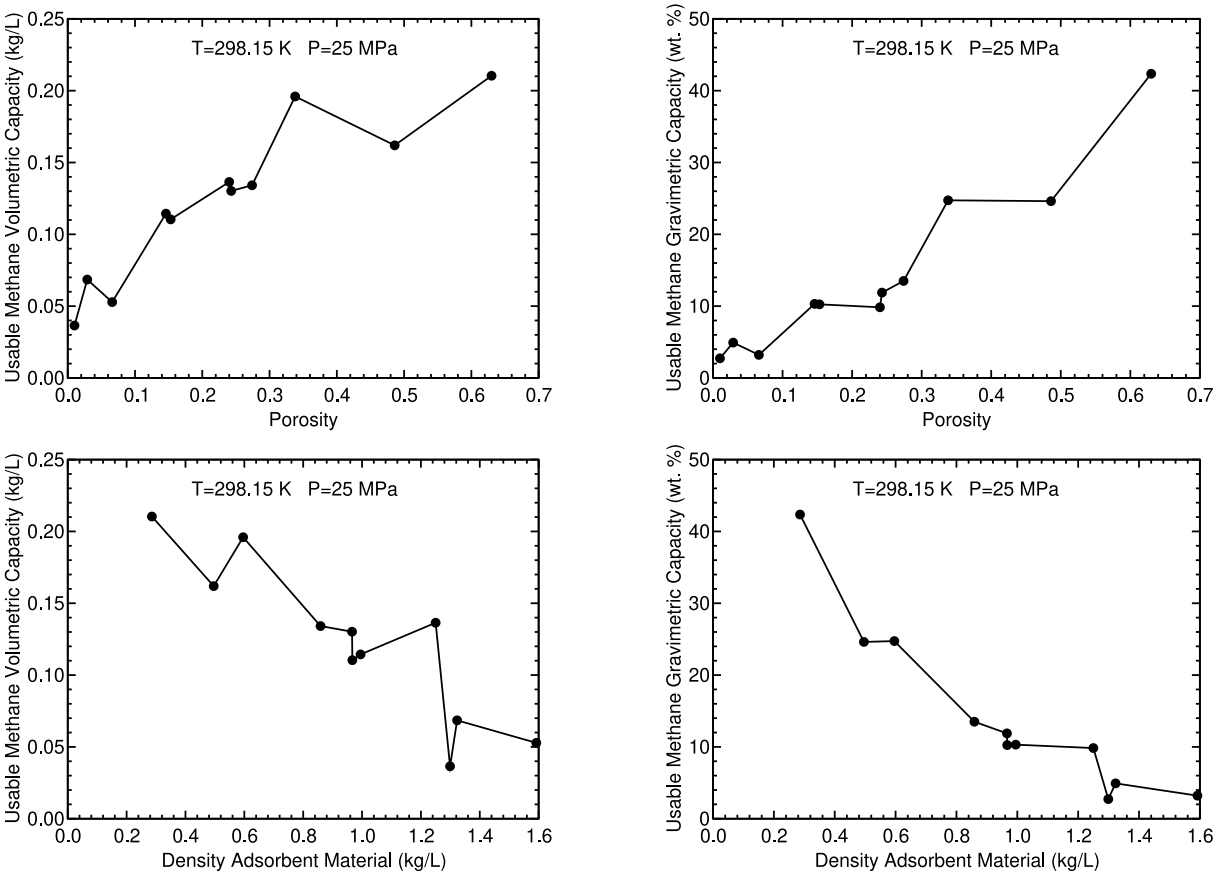

Fig. 10 – Useable methane volumetric and gravimetric capacities of BUTs at 298.15 K and 25 MPa vs their porosities (upper panels) and densities (lower panels).

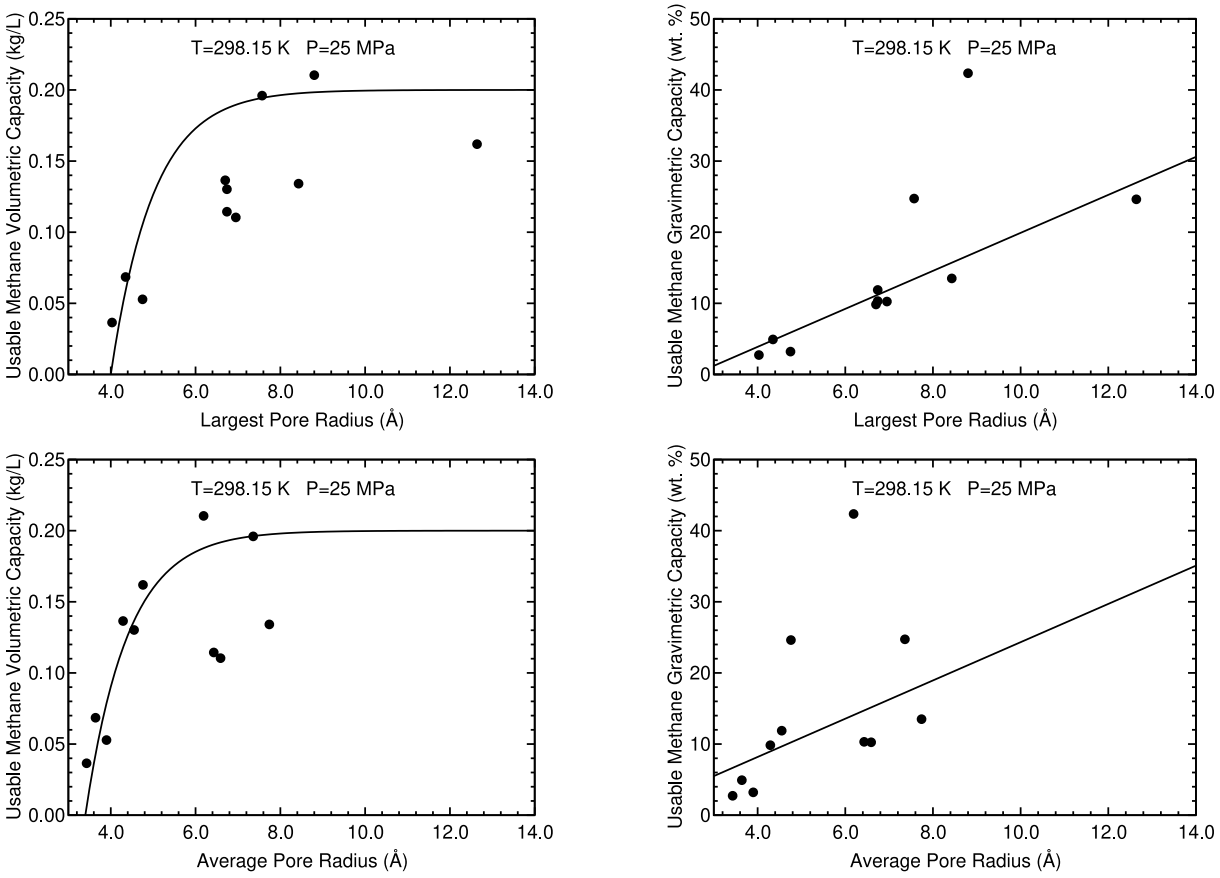

Fig. 11 – Useable methane volumetric and gravimetric capacities of BUTs at room temperature and 25 MPa vs their largest pore radius (upper panels) and average pore radius (lower panels).

and moderate pressures are usually below 2 wt % [33]. At pressures of 8 and 10 MPa the gravimetric capacities of MOFs are between 0.4 and 4 wt % [33]. The gravimetric capacities of the three BUTs at room temperature and 10 MPa are between 1.32 and 2.56 wt %, within that range of values.

It can be noticed in Fig. 9 that the useable gravimetric capacity of BUT-107 reaches the DOE 2025 gravimetric target, 5.5 wt %, at room temperature and pressures larger than approximately 27 MPa. The useable hydrogen gravimetric capacities of BUT-104 and 105 at 50 MPa and 298.15 K are very high, about 4 wt %. However, these gravimetric capacities are still below the DOE 2025 target.

GCMC methane storage capacities of BUTs

Methane storage capacities vs porosity, density and pore size

The useable methane storage capacities obtained in the GCMC simulations at 298.15 K and 25 MPa are tabulated in Table 6 and plotted in Fig. 10, as functions of the density and porosity of the BUTs. BUT-104, 105 and 107 have the highest methane storage capacities. Five BUTs have volumetric and gravimetric capacities in the ranges of 0.011–0.014 kg/L and 9.8–13.5 wt %, respectively. Three BUTs (102, 103 and 106) have volumetric and gravimetric capacities below 0.007 kg/L and 5 wt %, respectively.

According to Table 6 and Fig. 10, there are approximate correlations between the methane capacities and the porosity and the density, and they are similar to the ones obtained for hydrogen: The capacities increase as the porosity increases, they are inversely proportional to the density and the BUTs with the highest methane capacities have porosities above 0.4 and densities smaller than 0.6 kg/L.

The dependence of the useable methane v_c and g_c of the BUTs on the largest and average pore radius have been plotted in Fig. 11. It is similar to the dependence of the useable hydrogen capacities. The methane v_c increases fast as the radius increases and reaches a constant value. The methane g_c, excluding the methane gravimetric capacity of BUT-107, which is an outlier due to its low density, also increases with the radius R, but it increases linearly.

Isosteric heat of methane adsorption

The isosteric heat of methane adsorption at 273.15–353.15 K of zeolites, activated carbons and several carbon-based nanostructures is between 0.05 and 0.30 eV [80–86]. Zeolites have methane isosteric heats in the range 0.16–0.30 at temperatures of 273.15–353.15 K [83–86]. Ning et al. reported methane isosteric heats of 0.052–0.233 eV on activated carbons at room temperature [82]. Zhu and Zheng found that the methane isosteric heat at 298.15 K on graphene sheets,

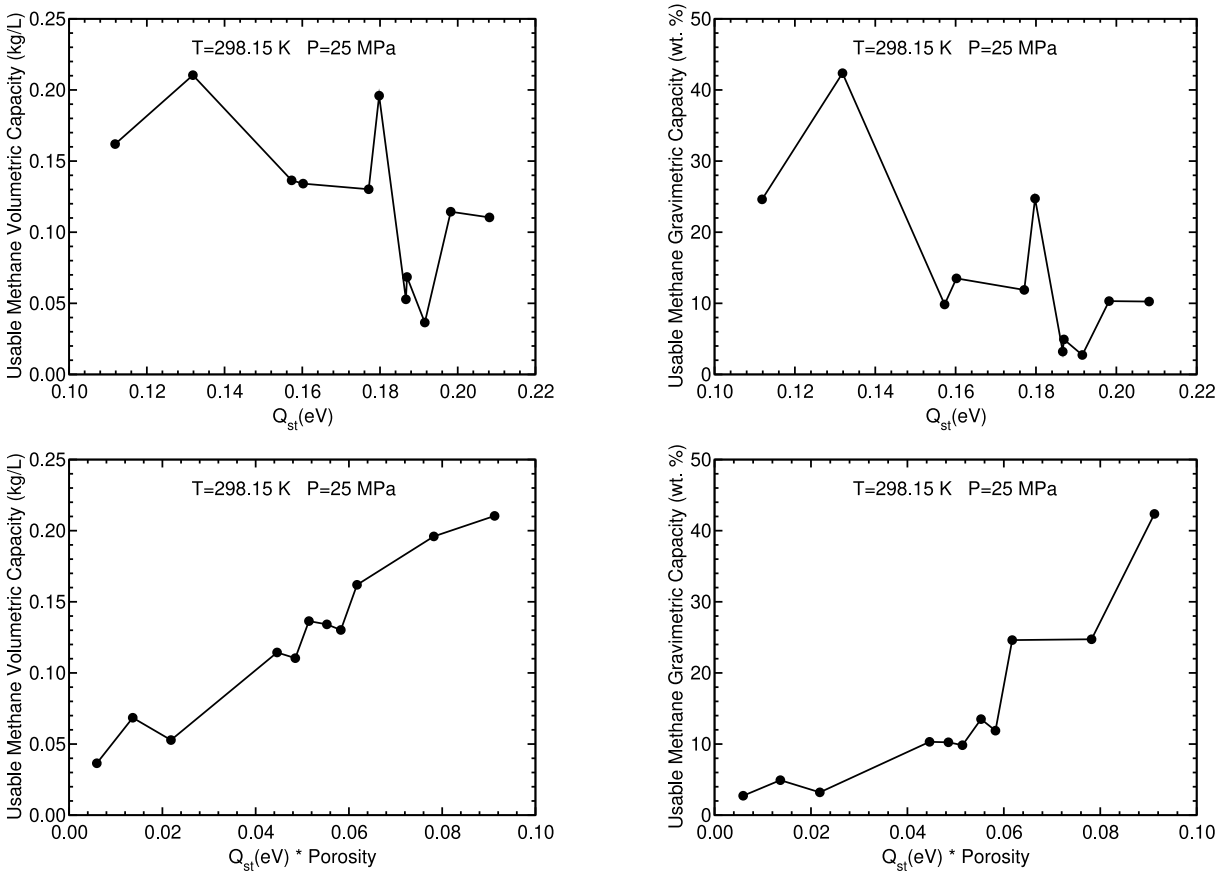

Fig. 12 – Useable methane volumetric and gravimetric capacities vs isosteric heat (upper panels) and vs isosteric heat multiplied by porosity (lower panels) at room temperature and 25 MPa of the novel BUTs.

Table 7 – Methane isosteric heat (in eV) of several solid porous materials. Temperature is in K.

Material	Q_{st}	Temperature	Source
Zeolites	0.16–0.30	273.15–353.15	[83–86]
Activated carbons	0.05–0.23	273.15–323.15	[80–82]
Graphene sheets	0.20	298.15	[81]
Carbon black	0.13	298.15	[81]
MOFs	0.03–0.31	298–304	[87,88]
BUTs	0.11–0.21	298.15	Present work

activated carbon and carbon black is 0.2017, 0.2274 and 0.1298 eV, respectively [81]. Recently, Abdulsalam et al. obtained that the methane isosteric heat of two activated carbons derived from South African coal at 273.15–323.15 K is in the range of 0.10–0.18 eV [80].

Regarding MOFs, the experimental isosteric heat of methane adsorption of MOFs at room temperature is between 0.03 and 0.31 eV [87,88] (See Table 7). Pribylov et al. [87] measured the average isosteric heat of methane at 303 K on three MOFs, Z205, Al-BTC (1,3,5-benzenetricarboxylate) and C300, and they obtained values of 0.0307, 0.1064 and 0.1375 eV, respectively. Z205, Al-BTC and C300 contain zinc, aluminum and copper, respectively. The isosteric heats of methane adsorption of the novel BUTs at 298.15 K and 25 MPa obtained in the present GCMC simulations are in the range 0.11–0.21 eV, similar to the isosteric heats of zeolites, activated carbons, carbon-based nanostructures and other MOFs (See Table 7).

The plot of the useable methane storage capacities vs the isosteric heat of the novel BUTs does not show any correlation between these magnitudes (See Fig. 12). In order to have high storage capacities, a large isosteric heat and large pore volume are necessary. Fig. 12 contains also a plot of the useable methane storage capacities vs the product of the isosteric heat, Q_{st}, and the porosity of the novel BUTs. It can be noticed in that figure that there is an approximate correlation between the storage capacities and the mentioned product of magnitudes. This means that the porosity must also be considered in order to understand the methane storage capacities.

The useable methane gravimetric capacity also depends on the density of the adsorbent material (See Eq. (6)). The useable methane v_c of the novel BUTs is much smaller than ρ_{ads}, except for BUT-104, 105 and 107. The g_c of the novel BUTs has been plotted vs Q_{st}/ρ_{ads} and the product of porosity and Q_{st}/ρ_{ads} in Fig. 13. There is not a correlation between g_c and Q_{st}. However, there is an approximate relationship between g_c and Q_{st}/ρ_{ads}: g_c is approximately proportional to Q_{st}/ρ_{ads}. There is an approximate correlation between the product of porosity and Q_{st}, but that correlation is higher between the product of the porosity and Q_{st}/ρ_{ads}. These facts indicate that the inclusion of the density of the adsorbent material is important to understand the gravimetric capacities.

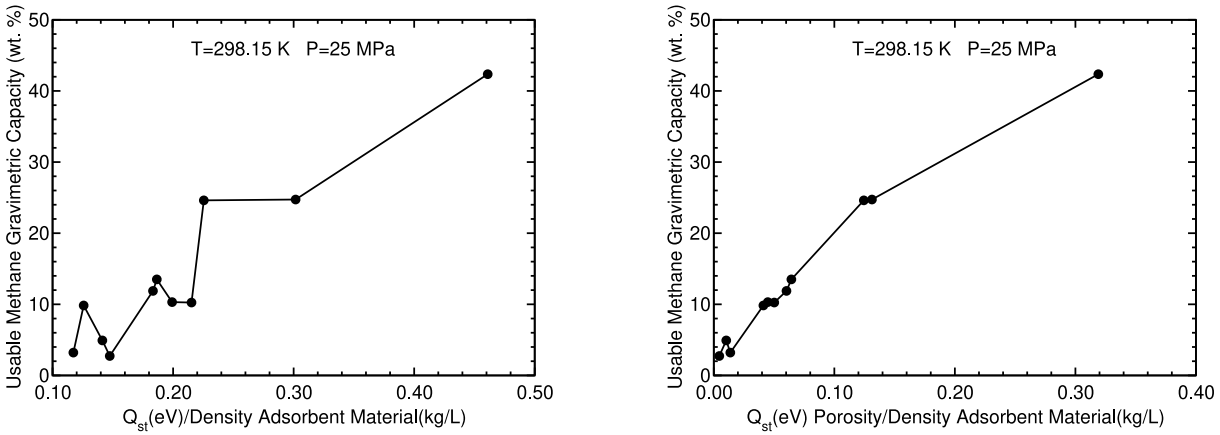

Fig. 13 – Useable methane gravimetric capacities vs Q_{st}/ρ_{ads} vs Q_{st}/ρ_{ads} multiplied by porosity at room temperature and 25 MPa of the novel BUTs.

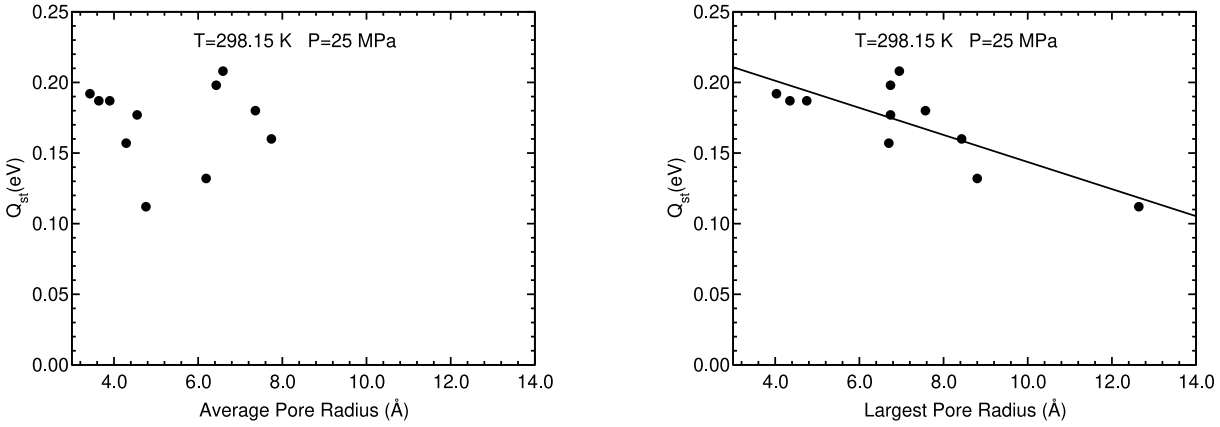

Fig. 14 – Methane isosteric heat (in eV) at 25 MPa and 298.15 K vs the average and largest pore radius (in Å) of the novel BUTs.

The dependence of the isosteric heat of methane on the largest and average pore radius (See Fig. 14) is similar to the dependence of the isosteric heat of hydrogen: There is not a clear dependence on the average pore radius and the isosteric heat decreases linearly as the largest pore radius increases.

Methane storage capacities vs pressure

GCMC simulations of the methane storage capacities of the three selected BUTs have been carried out at 298.15 K and pressures between 0.5 and 35 MPa. The results of the GCMC simulations are plotted in Fig. 15. The total methane volumetric capacities of BUT-104, 105 and 107 at 298.15 K and 4 MPa are 0.1428, 0.0616 and 0.0729 kg/L. According to experiments [26–28,31,35,36], the volumetric capacities at 298 K and 3.5–4 MPa of MOFs are between 0.0072 and 0.2146 kg/L, and the capacities of ACs are between 0.0358 and 0.1216 kg/L (See Table 8).

The total methane gravimetric capacities of BUT-104, 105 and 107 at 298.15 K and 4 MPa are 19.3, 11.0 and 20.2 wt %, respectively. Experimentally, the gravimetric capacities at 298 K and 3.5–4 MPa of MOFs are between 2.9 and 23 wt %, and the capacities of ACs are between 9 and 17 wt % (See Table 8). Hence, BUT-105 and 107 are among the MOFs with the highest methane gravimetric capacities at 4 MPa.

With regard to useable methane capacities, the results of the GCMC indicate that the useable methane v_c capacities of the three BUTs are high at moderate pressures, 25–35 MPa, between 0.16 and 0.23 kg/L, and close to the DOE methane volumetric target, 0.250 kg/L. The useable methane volumetric capacity of BUT-107 at 35 MPa is 0.230 kg/L, very close to the target. At 50 MPa, the useable methane v_c capacity reaches 0.250 kg/L, the DOE methane target. The useable gravimetric capacities of BUT-104 and 105 at 25–35 MPa are about 25 wt %, close to the DOE methane target, 33.33 wt %. The useable gravimetric capacity of BUT-107 reaches the DOE methane target at pressures equal or larger than approximately 9 MPa.

One reason of the higher capacities of BUT-107 is that its isotherms saturate (reach a constant value) at higher pressures than the isotherms of the other BUTs. The saturation feature has to do with its larger porosity (See Table 6). The shape of the volumetric capacity of BUT-107 as a function of the pressure suggests that this material has larger capacities at pressures larger than 35 MPa. Additional GCMC simulations at 50 MPa of BUT-107 yielded a useable volumetric and

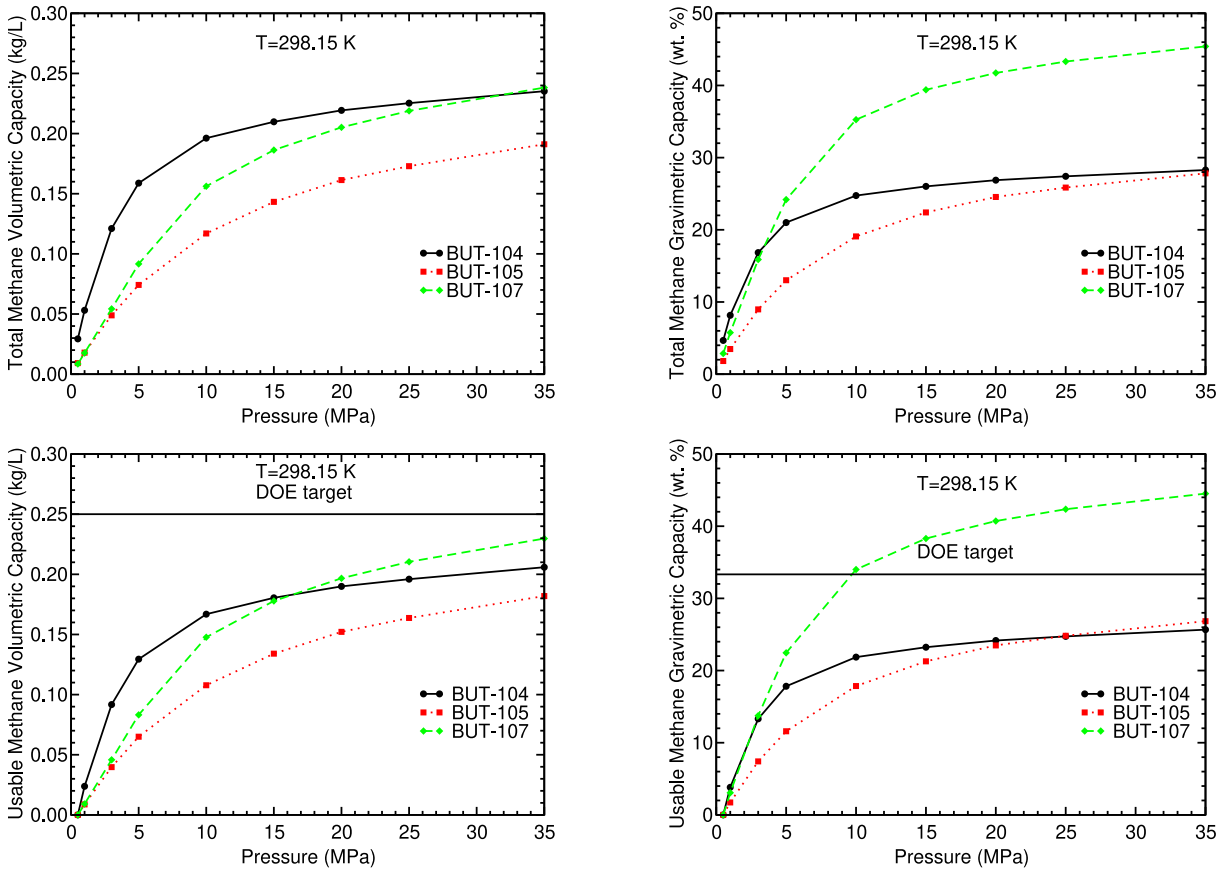

Fig. 15 – Total (upper panels) and useable (lower panels) methane volumetric and gravimetric capacities vs pressure at room temperature of three selected BUTs.

Table 8 – Total methane volumetric (in kg/L) and gravimetric (in wt. %) storage capacities of several solid porous materials. Temperature and pressure are in K and MPa, respectively.

Material	v_c	g_c	T	P	Source
ACs	0.0358–0.1216	9–17	298	3.5–4	[26–28, 31, 35, 36]
MOFs	0.0072–0.2146	2.9–23	298	3.5–4	[26–28, 31, 35, 36]
BUT-104, 105 and 107	0.0616–0.1428	11–20	298.15	4	Present work

gravimetric capacity of 0.2494 kg/L and 46.6 wt %, respectively, reaching the two DOE methane targets.

Conclusions

GCMC simulations of the total and useable hydrogen and methane storage capacities of eleven novel BUT MOFs have been carried out at 298.15 K and pressures between 0.5 and 50 MPa. The hydrogen and methane isosteric heats of the novel BUTs have been also calculated in the simulations. The present total and useable storage capacities are predictions that can be useful for experiments. The storage capacities have been analyzed as functions of the porosity, the density and the isosteric heat.

The analysis of the useable volumetric and gravimetric storage capacities of hydrogen and methane of the novel BUTs shows that these capacities are approximately correlated with the porosity and the density of the adsorbent material. There are no correlations between the isosteric heat of adsorption of hydrogen and methane and their corresponding storage capacities. If the analysis considers also the isosteric heat then, a higher correlation is found. The useable hydrogen and methane v_c and the product of the porosity and Q_{st} of the novel BUTs are highly correlated. As regards the useable hydrogen and methane g_c, the analysis of these capacities indicates that they are highly correlated with the product of the porosity and Q_{st}/ρ_{ads}.

Among the novel BUTs studied BUT-104, 105 and 107 have high hydrogen and methane storage capacities. The useable hydrogen volumetric capacities of the three BUTs are between 0.023 and 0.027 kg/L at 50 MPa, close to the DOE 2020 target, 0.030 kg/L, but they are about a 30–60% below the DOE 2025 hydrogen target, 0.040 kg/L. The useable hydrogen gravimetric capacities of BUT-104 and 105 at 50 MPa are very high, about 4 wt %, but below the DOE 2025 target, 5.5 wt %. An interesting

result is that the useable hydrogen gravimetric capacity of BUT-107 reaches the DOE 2025 target at 27 MPa.

As regards methane storage capacities, the useable methane gravimetric and volumetric capacities of BUT-104 and 105 at 25–35 MPa are about 25 wt % and 0.16–0.21 kg/L, close to the respective DOE methane targets, 33.33 wt % and 0.25 kg/L. The useable methane gravimetric and volumetric capacities of BUT-107 are 44 wt % and 0.23 kg/L at 35 MPa, respectively. According to the present simulations, BUT-107 reaches the two DOE methane targets at room temperature and 50 MPa and hence, this is a not expensive and suitable adsorbent material for adsorbed natural gas vehicles.

To enhance the hydrogen and methane storage capacities of these materials, one promising approach is the doping of Li and/or other light metals. These dopants have the ability to interact stronger with hydrogen and methane molecules, leading to enhanced adsorption and storage. Through careful selection and optimization of the doping process, the storage capacities of these materials can be effectively enhanced, opening up new possibilities for advanced gas storage applications.

Declaration of competing interest

The authors declare that they have no known competing financial interests or personal relationships that could have appeared to influence the work reported in this paper.

Acknowledgment

This work was founded by a research project from the Spain Ministry of Science, Innovation and Universities (MICINN) (Grant PGC2018-093745-B-I00), Junta de Castilla y León (Grant VA124G18) and the University of Valladolid, Spain. The use of the computer facilities of Centro de Proceso de Datos - Parque Científico of the University of Valladolid is acknowledged.

REFERENCES

[1] News European Parliament. CO_2 emissions from cars: facts and figures (infographics). https://www.europarl.europa.eu/news/en/headlines/society/20190313STO31218/co2-emissions-from-cars-facts-and-figures-infographics. [Accessed 20 June 2023]. 14 February.
[2] Office of Energy Efficiency & Renewable Energy, Fuel Cell Technologies Office. Materials-based hydrogen storage. https://www.energy.gov/eere/fuelcells/materials-based-hydrogen-storage. [Accessed 20 June 2023].
[3] Office of Energy Efficiency & Renewable Energy, Fuel Cell Technologies Office. DOE technical targets for onboard hydrogen storage for light-duty vehicles. https://www.energy.gov/eere/fuelcells/doe-technical-targets-onboard-hydrogen-storage-light-duty-vehicles. [Accessed 20 June 2023].
[4] Hua TQ, Roh HS, Ahluwalia RK. Performance assessment of 700-bar compressed hydrogen storage for light duty fuel cell vehicles. Int J Hydrogen Energy 2017;42:25121–9. https://doi.org/10.1016/j.ijhydene.2017.08.123.
[5] Advanced Research Projects Agency - Energy, DOE. Methane opportunities for vehicular energy (MOVE) program overview. https://arpa-e.energy.gov/technologies/programs/move. [Accessed 20 June 2023].
[6] Chen Z, Kirlikovali KO, Idrees KB, Wasson MC, Farha OK. Porous materials for hydrogen storage. Chem 2022;8:693–716. https://doi.org/10.1016/j.chempr.2022.01.012.
[7] Hynek S, Fuller W, Bentley J. Hydrogen storage by carbon sorption. Int J Hydrogen Energy 1997;22:601–10.
[8] Alali I, Mokaya R. Direct synthesis of organic salt-derived porous carbons for enhanced CO_2 and methane storage. J Mater Chem 2023;11:6952–65. https://doi.org/10.1039/D3TA00044C.
[9] Blankenship LS, Mokaya R. Modulating the porosity of carbons for improved adsorption of hydrogen, carbon dioxide, and methane: a review. Mater Adv 2022;3:1905. https://doi.org/10.1039/d1ma00911g.
[10] Attia NF, Jung M, Park J, Cho SY, Oh H. Facile synthesis of hybrid porous composites and its porous carbon for enhanced H_2 and CH_4 storage. Int J Hydrogen Energy 2020;45:32797–807.
[11] Jung M, Park J, Lee K, Attia NF, Oh H. Effective synthesis route of renewable nanoporous carbon adsorbent for high energy gas storage and CO_2/N_2 selectivity. Renew Energy 2020;161:30–42. https://doi.org/10.1016/j.renene.2020.06.125.
[12] Attia NF, Jung M, Park J, Jang H, Lee K, Oh H. Flexible nanoporous activated carbon cloth for achieving high H_2, CH_4, and CO_2 storage capacities and selective CO_2/CH_4 separation. Chem Eng J 2020;379:122367. https://doi.org/10.1016/j.cej.2019.122367.
[13] Park J, Jung M, Jang H, Lee K, Attia NF, Oh H. A facile synthesis tool of nanoporous carbon for promising H_2, CO_2, and CH_4 sorption capacity and selective gas separation. J Mater Chem 2018;6:23087–100.
[14] de Almeida Neto GR, Matheus FH, Gonçalves Beatrice CA, Leiva DR, Pessan LA. Fundamentals and recent advances in polymer composites with hydride-forming metals for hydrogen storage applications. Int J Hydrogen Energy 2022;47:34139–64. https://doi.org/10.1016/j.ijhydene.2022.08.004.
[15] Attia NF, Geckeler KE. Polyaniline–polypyrrole composites with enhanced hydrogen storage capacities. Macromol Rapid Commun 2013;34:931–7. https://doi.org/10.1002/marc.201300060.
[16] Tian M, Rochat S, Fawcett H, Burrows AD, Bowen CR, Mays TJ. Chemical modification of the polymer of intrinsic microporosity PIM-1 for enhanced hydrogen storage. Adsorption 2020;26:1083–91. https://doi.org/10.1007/s10450-020-00239-y.
[17] Wang Z, Li XM, Li H. Stable and microporous covalent organic frameworks via weak interactions for gas uptake. CrystEngComm 2023;25:1910–4. https://doi.org/10.1039/D2CE01645A.
[18] Dong Y, Zhang X, Wang Y, Tang L, Yang Y. Engineering building blocks of covalent organic frameworks for boosting capacitive charge storage. J Power Sources 2023;564:232873. https://doi.org/10.1016/j.jpowsour.2023.232873.
[19] Moosavi SM, Nandy A, Jablonka KM, Ongari D, Janet JP, Boyd PG, et al. Understanding the diversity of the metal-organic framework ecosystem. Nat Commun 2020;11:4068. https://doi.org/10.1038/s41467-020-17755-8.
[20] Liu Y, Shen D, Tu Z, Xing L, Chung YG, Li S. Room-temperature hydrogen storage performance of metal-organic framework/graphene oxide composites by molecular simulations. Int J Hydrogen Energy 2022;47:41055–68.
[21] Shet SP, Priya SS, Sudhakar K, Tahir M. A review on current trends in potential use of metal-organic framework for hydrogen storage. Int J Hydrogen Energy 2021;46:11782–803. https://doi.org/10.1016/j.ijhydene.2021.01.020.

[22] Yu S, Jing G, Li S, Li Z, Ju X. Tuning the hydrogen storage properties of MOF-650: a combined DFT and GCMC simulations study. Int J Hydrogen Energy 2020;45:6757–64.
[23] Cabria I, Suárez-García F, Mazadiego LF, Ortega MF. Methane storage in nanoporous carbons. 21st Century Nanoscience – A Handbook: Low-Dimensional Materials and Morphologies 2020;4:1–14. https://doi.org/10.1201/9780429347290. chap. 23. Boca Raton: CRC Press.
[24] Ahmed A, Liu Y, Purewal J, Tran LD, Wong-Foy AG, Veenstra M, et al. Balancing gravimetric and volumetric hydrogen density in MOFs. Energy Environ Sci 2017;10:2459–71. https://doi.org/10.1039/C7EE02477K.
[25] Kumar KV, Preuss K, Titirici M, Rodríguez-Reinoso F. Nanoporous materials for the onboard storage of natural gas. Chem Rev 2017;117:1796–825.
[26] Alhasan S, Carriveau R, Ting DSK. A review of adsorbed natural gas storage technologies. Int J Environ Stud 2016;73:343–56.
[27] Beckner M, Dailly A. Adsorbed methane storage for vehicular applications. Appl Energy 2015;149:69–74.
[28] Liu B, Wang W, Wang N, Au CT. Preparation of activated carbon with high surface area for high-capacity methane storage. J Energy Chem 2014;23:662–8.
[29] Pham T, Forrest KA, Hogan A, Mclaughlin K, Belof JL, Eckert J, et al. Simulations of hydrogen sorption in rht-MOF-1: identifying the binding sites through explicit polarization and quantum rotation calculations. J Mater Chem 2014;2:2088–100. https://doi.org/10.1039/c3ta14591c.
[30] Langmi HW, Ren J, North B, Mathe M, Bessarabov D. Hydrogen storage in metal-organic frameworks: a review. Electrochim Acta 2014;128:368–92.
[31] Makal TA, Li JR, Lu W, Zhou HC. Methane storage in advanced porous materials. Chem Soc Rev 2012;41:7761–79.
[32] Stern AC, Belof JL, Mohamed E, Brian S. Understanding hydrogen sorption in a polar metal-organic framework with constricted channels. J Chem Phys 2012;136:15202–98.
[33] Hu YH, Zhang L. Hydrogen storage in metal-organic frameworks. Adv Mater 2010;22:E117–30. https://doi.org/10.1002/adma.200902096.
[34] Frost H, Düren T, Snurr RQ. Effects of surface area, free volume, and heat of adsorption on hydrogen uptake in metal-organic frameworks. J Phys Chem B 2006;110:9565–70. https://doi.org/10.1021/jp060433+.
[35] Lozano-Castelló D, Cazorla-Amorós D, Linares-Solano A, Quinn DF. Influence of pore size distribution on methane storage at relatively low pressure: preparation of activated carbon with optimum pore size. Carbon 2002;40:989–1002.
[36] Vasiliev LL, Kanonchik L, Mishkinis DA, Rabetsky MI. Adsorbed natural gas storage and transportation vessels. Int J Therm Sci 2000;39:1047–55.
[37] Kong XJ, He T, Zhang YZ, Wu XQ, Wangn SN, Xu MM, et al. Constructing new metal-organic frameworks with complicated ligands from "one-pot" in situ reactions. Chem Sci 2019;10:3949–55. https://doi.org/10.1039/c9sc00178f.
[38] Metropolis N. The beginning of the Monte Carlo method. Los Alamos Sci 1987;15:125–30.
[39] Soave G. Equilibrium constants from a modified Redlich-Kwong equation of state. Chem Eng Sci 1972;27:1197–203.
[40] Zhou L, Zhou Y. Determination of compressibility factor and fugacity coefficient of hydrogen in studies of adsorptive storage. Int J Hydrogen Energy 2001;26:597–601.
[41] Xu XH, Duan YY, Yang Z. Crossover volume translation Soave-Redlich-Kwong equation of state for fluids. Ind Eng Chem Res 2012;51:6580–5.
[42] Lennard-Jones JE. On the determination of molecular fields. Proc Roy Soc (London) A 1924;106:463–77. https://doi.org/10.1098/rspa.1924.0082.
[43] Good RJ, Hope CJ. New combining rule for intermolecular distances in intermolecular potential functions. J Chem Phys 1970;53:540–3. https://doi.org/10.1063/1.1674022.
[44] Berthelot D. Sur le mélange des gaz. Comptes rendus hebdomadaires des séances de l'Académie des Sciences 1898;126:1703.
[45] Rzepka M, Lamp P, de la Casa-Lillo MA. Physisorption of hydrogen on microporous carbon nanotubes. J Phys Chem B 1998;102:10894–8.
[46] Feynman RP, Hibbs A. Quantum mechanics and path integrals. New York: McGraw-Hill; 1965.
[47] Baowan D, Hill JM. Nested boron nitride and carbon-boron nitride nanocones. Micro & Nano Lett 2007;2:46–9.
[48] Tu Y, Xiu P, Wan R, Hu J, Zhou R, Fang H. Water-mediated signal multiplication with Y-shaped carbon nanotubes. Proc Natl Acad Sci USA 2009;106:18120–4.
[49] Tribe L, Manning M, Morgan JA, Stephens MD, Ronk WR, Treptow E, et al. Argon scattering off the surface of liquid indium: exit angle and energy dependence. J Phys Chem B 1998;102:206–11.
[50] de Araujo AS, Sonoda MT, Piro OE, Castellano EE. Development of new Cd^{2+} and Pb^{2+} Lennard-Jones parameters for liquid simulations. J Phys Chem B 2007;111:2219–24.
[51] Sebesta F, Sláma V, Melcr J, Futera Z, Burda JV. Estimation of transition-metal empirical parameters for molecular mechanical force fields. J Chem Theor Comput 2016;12:3681–8. https://doi.org/10.1021/acs.jctc.6b00416.
[52] Filippova VP, Kunavin SA, Pugachev MS. Calculation of the parameters of the Lennard-Jones potential for pairs of identical atoms based on the properties of solid substances. Inorg Mater: Applied Research 2015;6:1–4.
[53] Cheung PSY, Powles JG. The properties of liquid nitrogen. Mol Phys 1975;30:921–49.
[54] Jorgensen WL, Madura JD, Swenson CJ. Optimized intermolecular potential functions for liquid hydrocarbons. J Am Chem Soc 1984;106:6638–46.
[55] Mayo SL, Olafson BD, Goddard III WA. DREIDING: a generic force field. J Phys C Solid State Phys 1990;94:8897–909.
[56] Rappé AK, Casewit CJ, Colwell KS, Goddard III WA, Skiff WM. UFF, a full periodic table force field for molecular mechanics and molecular dynamics simulations. J Am Chem Soc 1992;114:10024–35. https://doi.org/10.1021/ja00051a040.
[57] Soper AK. The structure of molten $ZnCl_2$: a new analysis of some old data. Pramana - J Phys 2004;63:41–50.
[58] Beyer O, Hoheisel C. Molecular dynamics studies on the structure of binary metallic glasses based on Lennard-Jones(12-6)potentials. I. $Ni_{81}B_{19}$ and $Cu_{57}Zr_{43}$. Z Naturforsch 1983;38:859–65. https://doi.org/10.1515/zna-1983-0808.
[59] Caviedes D, Cabria I. Grand canonical Monte Carlo simulations of the hydrogen storage capacities of slit-shaped pores, nanotubes and torusenes. Int J Hydrogen Energy 2022;47:11916–28. https://doi.org/10.1016/j.ijhydene.2022.01.229.
[60] Papadimitriou NI, Tsimpanogiannis IN, Stubos AK. Monte Carlo study of sI hydrogen hydrates. Mol Simulat 2010;36:736–44. https://doi.org/10.1080/08927021003752796.
[61] Allen MP, Tildesley DJ. Computer simulation of liquids. Oxford: Oxford University Press; 1987.
[62] Broom DP, Webb CJ, Fanourgakis GS, Froudakis GE, Trikalitis PN, Hirscher M. Concepts for improving hydrogen storage in nanoporous materials. Int J Hydrogen Energy 2019;44:7768–79.
[63] Allendorf MD, Hulvey Z, Gennett T, Ahmed A, Autrey T, Camp J, et al. An assessment of strategies for the development of solid-state adsorbents for vehicular hydrogen storage. Energy Environ Sci 2018;11:2784–812. https://doi.org/10.1039/C8EE01085D.

[64] Schlichtenmayer M, Hirscher M. The useable capacity of porous materials for hydrogen storage. Appl Phys A 2016;122:379. https://doi.org/10.1007/s00339-016-9864-6.
[65] Cambridge Crystallographic Database Centre. www.ccdc.cam.ac.uk. [Accessed 20 June 2023].
[66] Jaramillo DE, Jiang HZH, Evans HA, Chakraborty R, Furukawa H, Brown CM, et al. Ambient-temperature hydrogen storage via vanadium(II)-dihydrogen complexation in a metal-organic framework. J Am Chem Soc 2021;143:6248–56. https://doi.org/10.1021/jacs.1c01883.
[67] Denysenko D, Grzywa M, Jelic J, Reuter K, Volkmer D. Scorpionate-type coordination in MFU-4l metal-organic frameworks: small-molecule binding and activation upon the thermally activated formation of open metal sites. Angew Chem Int Ed 2014;53:5832–6. 0.1002/anie.201310004.
[68] Bhatia SK, Myers AL. Optimum conditions for adsorptive storage. Langmuir 2006;22:1688–700.
[69] Lochan R, Head-Gordon M. Computational studies of molecular hydrogen binding affinities: the role of dispersion forces, electrostatics, and orbital interactions. Phys Chem Chem Phys 2006;8:1357–70.
[70] Li J, Furuta T, Goto H, Ohashi T, Fujiwara Y, Yip S. Theoretical evaluation of hydrogen storage capacity in pure carbon nanostructures. J Chem Phys 2003;119:2376–85.
[71] Bae YS, Snurr RQ. Optimal isosteric heat of adsorption for hydrogen storage and delivery using metal organic frameworks. Microporous Mesoporous Mater 2010;132:300–3.
[72] Ipek B, Altiparmak I. Remarkable isosteric heat of hydrogen adsorption on Cu(I)-exchanged SSZ-39. Int J Hydrogen Energy 2020;45:34972–82. https://doi.org/10.1016/j.ijhydene.2020.03.083.
[73] Ipek B, Pollock RA, Brown CM, Uner D, Lobo RF. H_2 adsorption on Cu(I)–SSZ-13. J Phys Chem C 2018;122:540–8. https://doi.org/10.1021/acs.jpcc.7b09963.
[74] Blankenship LS, Balahmar N, Mokaya R. Oxygen-rich microporous carbons with exceptional hydrogen storage capacity. Nat Commun 2017;8:1545. https://doi.org/10.1038/s41467-017-01633-x.
[75] Schaefer S, Fierro V, Izquierdo MT, Celzard A. Assessment of hydrogen storage in activated carbons produced from hydrothermally treated organic materials. Int J Hydrogen Energy 2016;41:12146–56.
[76] Frost H, Snurr RQ. Design requirements for metal-organic frameworks as hydrogen storage materials. J Phys Chem C 2007;111:18794–803. https://doi.org/10.1021/jp076657p.
[77] Kunowsky M, Lozar JPM, Amoros DC, Solano AL. Scale-up activation of carbon fibres for hydrogen storage. Int J Hydrogen Energy 2010;35:2393–402. https://doi.org/10.1016/j.ijhydene.2009.12.151.
[78] Xu WC, Takahashi K, Matsuo Y, Hattori Y, Kumagai M, Ishiyama S, et al. Investigation of hydrogen storage capacity of various carbon materials. Int J Hydrogen Energy 2007;32:2504–12.
[79] Ströbel R, Jorissen L, Schliermann T, Trapp V, Schutz W, Bohmhammel K, et al. Hydrogen adsorption on carbon materials. J Power Sources 1999;84:221. https://doi.org/10.1016/S0378-7753(99)00320-1.
[80] Abdulsalam J, Mulopo J, Bada SO, Oboirien B. Equilibria and isosteric heat of adsorption of methane on activated carbons derived from south african coal discards. ACS Omega 2020;5:32530–9. https://doi.org/10.1021/acsomega.0c04744.
[81] Zhu ZW, Zheng QR. Methane adsorption on the graphene sheets, activated carbon, and carbon black. Appl Therm Eng 2016;108:605–13. https://doi.org/10.1016/j.applthermaleng.2016.07.146.
[82] Ning P, Li F, Yi H, Tang X, Peng J, Li Y, et al. Adsorption equilibrium of methane and carbon dioxide on microwave activated carbon. Sep Purif Technol 2012;98:321–6.
[83] Pillai RS, Peter SA, Jasra RV. Adsorption of carbon dioxide, methane, nitrogen, oxygen, and argon in NaETS-4. Microporous Mesoporous Mater 2008;113:268–76.
[84] Himeno S, Tomita T, Suzuki K, Yoshida S. Characterization and selectivity for methane and carbon dioxide adsorption on the all-silica DD3R zeolite. Microporous Mesoporous Mater 2007;98:62–9.
[85] Grey T, Travis K, Gale J, Nicholson D. A comparative simulation study of the adsorption of nitrogen and methane in siliceous heulandite and chabazite. Microporous Mesoporous Mater 2001;48:203–9.
[86] Choudhary VR, Mayadevi S. Adsorption of methane, ethane, ethylene, and carbon dioxide on silicalite-I. Zeolites 1996;17:501–7.
[87] Pribylov AA, Murdmaa KO, Solovtsova OV, Knyazeva MK. Methane adsorption on various metal-organic frameworks and determination of the average adsorption heats at supercritical temperatures and pressures. Russ Chem Bull 2018;67:1807–13. https://doi.org/10.1007/s11172-018-2293-2.
[88] Zhou W. Methane storage in porous metal-organic frameworks: current records and future perspectives. Chem Rec 2010;10:200–4. https://doi.org/10.1002/tcr.201000004.